2015

Structure and functional characterization of a bile acid 7 alpha dehydratase BaiE in secondary bile acid synthesis

Shiva Bhowmik
The Scripps Research Institute

Hsien-Po Chiu
Genomics Institute of Novartis Research Foundation

David H. Jones
Genomics Institute of Novartis Research Foundation

Hsiu-Ju Chiu
SLAC National Accelerator Laboratory

Mitchell D. Miller
SLAC National Accelerator Laboratory

See next page for additional authors

Proteins: Structure, Function, and Bioinformatics

Article first published online : 18 JAN 2016, DOI: 10.1002/prot.24971

Structure and functional characterization of a bile acid 7α dehydratase BaiE in secondary bile acid synthesis

Shiva Bhowmik,[1,2] Hsien-Po Chiu,[3] David H. Jones,[3] Hsiu-Ju Chiu,[1,4] Mitchell D. Miller,[1,4] Qingping Xu,[1,4] Carol L. Farr,[1,2] Jason M. Ridlon,[5,6] James E. Wells,[7] Marc-André Elsliger,[1,2] Ian A. Wilson,[1,2] Phillip B. Hylemon,[5,6] and Scott A. Lesley[1,2,3]*

[1] Joint Center for Structural Genomics, (http://www.jcsg.org)

[2] Department of Integrative Structural and Computational Biology, The Scripps Research Institute, 10550 North Torrey Pines Road, La Jolla, California, 92037

[3] Genomics Institute of Novartis Research Foundation, 10675 John Jay Hopkins Drive, San Diego, California, 92121

[4] Stanford Synchrotron Radiation Lightsource, SLAC National Accelerator Laboratory, 2575 Sand Hill Road, MS 9, Menlo Park, California, 94025

[5] Department of Microbiology and Immunology, Virginia Commonwealth University, Richmond, Virginia, 23298

[6] McGuire VA Medical Center, Richmond, Virginia, 23298

[7] USDA ARS, US Meat Animal Research Center, Clay Center, Nebraska, 68933

ABSTRACT

Conversion of the primary bile acids cholic acid (CA) and chenodeoxycholic acid (CDCA) to the secondary bile acids deoxycholic acid (DCA) and lithocholic acid (LCA) is performed by a few species of intestinal bacteria in the genus *Clostridium* through a multistep biochemical pathway that removes a 7α-hydroxyl group. The rate-determining enzyme in this pathway is bile acid 7α-dehydratase (*baiE*). In this study, crystal structures of apo-BaiE and its putative product-bound [3-oxo-$\Delta^{4,6}$-lithocholyl-Coenzyme A (CoA)] complex are reported. BaiE is a trimer with a twisted α + β barrel fold with similarity to the Nuclear Transport Factor 2 (NTF2) superfamily. Tyr30, Asp35, and His83 form a catalytic triad that is conserved across this family. Site-directed mutagenesis of BaiE from *Clostridium scindens* VPI 12708 confirm that these residues are essential for catalysis and also the importance of other conserved residues, Tyr54 and Arg146, which are involved in substrate binding and affect catalytic turnover. Steady-state kinetic studies reveal that the BaiE homologs are able to turn over 3-oxo-Δ^4-bile acid and CoA-conjugated 3-oxo-Δ^4-bile acid substrates with comparable efficiency questioning the role of CoA-conjugation in the bile acid metabolism pathway.

Proteins 2016; 00:000–000.

Key words: gut microbes; secondary bile acid synthesis; gut microbe mediated human metabolite; 7α-dehyroxylation; bile acid 7α-dehydratase; primary bile acid; secondary bile acid; nuclear transport factor-2 superfamily; structural genomics.

INTRODUCTION

The human gut microbiome is a key aspect of normal physiology and metabolic homeostasis. A large number of normal host functions and disease states have been associated with intestinal microbiota.[1–5] Understanding the interplay between host and microbe is a pivotal challenge since the underlying biochemical events are undefined. Metabolomics studies performed with germ-free

Abbreviations: CoA, coenzyme A; IBD, inflammatory bowel disease; LCA, lithocholic acid; NTF2, nuclear transport factor 2; 3-oxo-Δ^4-CDCA, 3-oxo-Δ^4-chenodeoxycholate; 3-oxo-$\Delta^{4,6}$-LCA, 3-oxo-$\Delta^{4,6}$-lithocholate; 3-oxo-Δ^4-CDC-CoA, 3-oxo-Δ^4-chenodeoxycholyl coenzyme A; 3-oxo-$\Delta^{4,6}$-LC-CoA, 3-oxo-$\Delta^{4,6}$-lithocholyl coenzyme A; TEV, tobacco etch virus

Grant sponsor: National Institutes of Health (NIH), National Institute of General Medical Sciences (NIGMS) Protein Structure Initiative; Grant number: U54 GM094586; Grant sponsor: VA Merit Award; Grant number: BX001328 (to PBH).
*Correspondence to: Scott A. Lesley; Department of Integrative Structural and Computational Biology, The Scripps Research Institute, 10550 North Torrey Pines Road, La Jolla, California, 92037. E-mail: slesley@scripps.edu
Received 24 July 2015; Revised 12 November 2015; Accepted 30 November 2015
Published online 9 December 2015 in Wiley Online Library (wileyonlinelibrary.com). DOI: 10.1002/prot.24971

and conventional mice have identified metabolites processed by microbes, which can influence human health.[6–8] Among such metabolites, secondary bile acids, deoxycholate (DCA) and lithocholate (LCA), which are synthesized from primary bile acids cholate and chenodeoxycholate, respectively, are associated with an increase in the incidence of cancers of the colon, esophagus, and biliary track as well as cholesterol gallstone disease in some patients.[9–12] Furthermore, recent studies of obesity-associated hepatocellular carcinoma (HCC) in mice, implicated DCA with increased secretion of various inflammatory and tumor promoting factors in the liver.[13] This study showed that blocking DCA production could prevent HCC in obese mice.

Bile acids also act as hormones via activating specific nuclear receptors (FXR, PXR, and vitamin D receptor) and plasma membrane G-protein coupled receptors [TGR-5, sphingosine-1-phosphate receptor 2, muscarinic M (2) receptor] in a physiologically relevant manner. Secondary bile acids are more powerful than primary bile acids as activators of PXR, Vitamin D receptor, and TGR-5 in cell signaling pathways.[14] In humans, unlike rodents, DCA can accumulate to very high levels (>60%) in the bile acid pool as the human liver is unable to hydroxylate DCA at the 7α-position.[15] Therefore, by controlling the composition of the bile acid pool, specific gut bacteria may influence aspects of host physiology and influence pathophysiology. Hence, the microbial enzymes involved in secondary bile acid synthesis are potential drug targets for human disease.

Microbial synthesis of secondary bile acids in the human gut involves a multistep biochemical process that results in the removal of *C7*-hydroxy group from primary bile acids (Fig. 1). This pathway, which is split into oxidative and reductive arms, involves a series of enzymes that are encoded by a bile acid inducible (*bai*) operon.[15] The pathway is initiated by the uptake of primary bile acid via a H^+-dependent active transporter (BaiG)[16] followed by thioesterification to coenzyme A (CoA) by a CoA-ligase (BaiB).[17] The oxidative arm of the pathway converts bile acid-CoA thioester to 3-oxo-7α-hydroxy bile acid-CoA and 3-oxo-Δ^4−7α-hydroxy bile acid-CoA intermediates by BaiA[18] and BaiCD,[19] respectively. The 7α-hydroxy group is removed from the latter through release of water by bile acid 7α dehydratase, BaiE, yielding a 3-oxo-$\Delta^{4,6}$-bile acid-CoA intermediate.[20] The subsequent three reductive steps catalyzed by yet unidentified enzymes constitute the reductive arm generating the secondary bile acid. Two CoA transferases, BaiF and BaiK, participate in the removal of the CoA moiety, although it remains unclear at which stage in the pathway this occurs.[21] Despite the significant influence of this pathway on human health and disease, limited structural and biochemical information is available for the key microbial enzymes involved. We recently reported the structural and steady-state kinetic characterization of BaiA2 from *Clostridium scindens* VPI 12708, which represents the first structure–function characterization of enzymes in this pathway.[22]

Here we report the structural and biochemical characterization of BaiE homologs from *Clostridium* sp. a key human gut microbe associated with secondary bile acid synthesis. The 7α-dehydroxylation step catalyzed by BaiE is rate limiting for this pathway and is the only irreversible step that directs the intermediate from the oxidative arm to the reductive arm generating the secondary bile acid. BaiE has less than 30% sequence identity with its nearest structural homolog. The BaiE crystal structure reveals a canonical twisted α + β barrel fold that is also observed in the Nuclear Transport Factor 2 (NTF2) family. Structure-guided site directed mutagenesis studies were carried out to identify and differentiate residues involved in substrate binding versus those specifically involved in catalysis. Furthermore, comparison of the co-crystal structure of BaiE from *Clostridium hiranonis* DSM13275 with the partially bound product [3-oxo-$\Delta^{4,6}$-Lithocholyl Coenzyme A (3-oxo-$\Delta^{4,6}$-LC-CoA)] with apo-structures of BaiE homologs revealed a dramatically different conformation of the loop formed by residues 48–63. This segment forms the roof of the active site pocket and suggests conformational flexibility may be needed for substrate binding. Site-directed mutagenesis of Tyr54 indicated impaired substrate turnover indicating the importance of this loop in catalysis. A mechanism for bile acid dehydratase catalysis is proposed based on structural features and site-directed mutagenesis studies. The insight from these structures should facilitate the design of inhibitors which could modulate levels of secondary bile acids in pathways associated with human health and disease.

MATERIALS AND METHODS

Gene cloning and site-directed mutagenesis

Genes of the BaiE homologs were cloned from the corresponding genomic DNAs of *C. scindens* VPI12708, *C. scindens* ATCC35704, *C. hylemonae* DSM15053, and *C. hiranonis* DSM13275 by Polymerase Incomplete Primer Extension (PIPE) cloning method.[23,24] *C. scindens* VPI12708 genomic DNA was isolated from anaerobically grown culture.[25] All other genomic DNAs were obtained from the DSMZ (Braunschweig, Germany). The genes were amplified by polymerase chain reaction (PCR) and cloned into the expression vector, pSpeedET, which also encodes an N-terminal tobacco etch virus (TEV) protease-cleavable expression and purification (MGSDKIHHHHHH-HENLYFQ/G). Expression clones for PDB ID: 4L8P, 4LEH, 4L8O, and 4N3V are available from the NIH PSI Materials Repository (http://psimr.asu.edu/MRLinks.html) Site-directed mutants were generated using the QuikChange™ Site-Directed Mutagenesis Kit (Agilent Technologies,

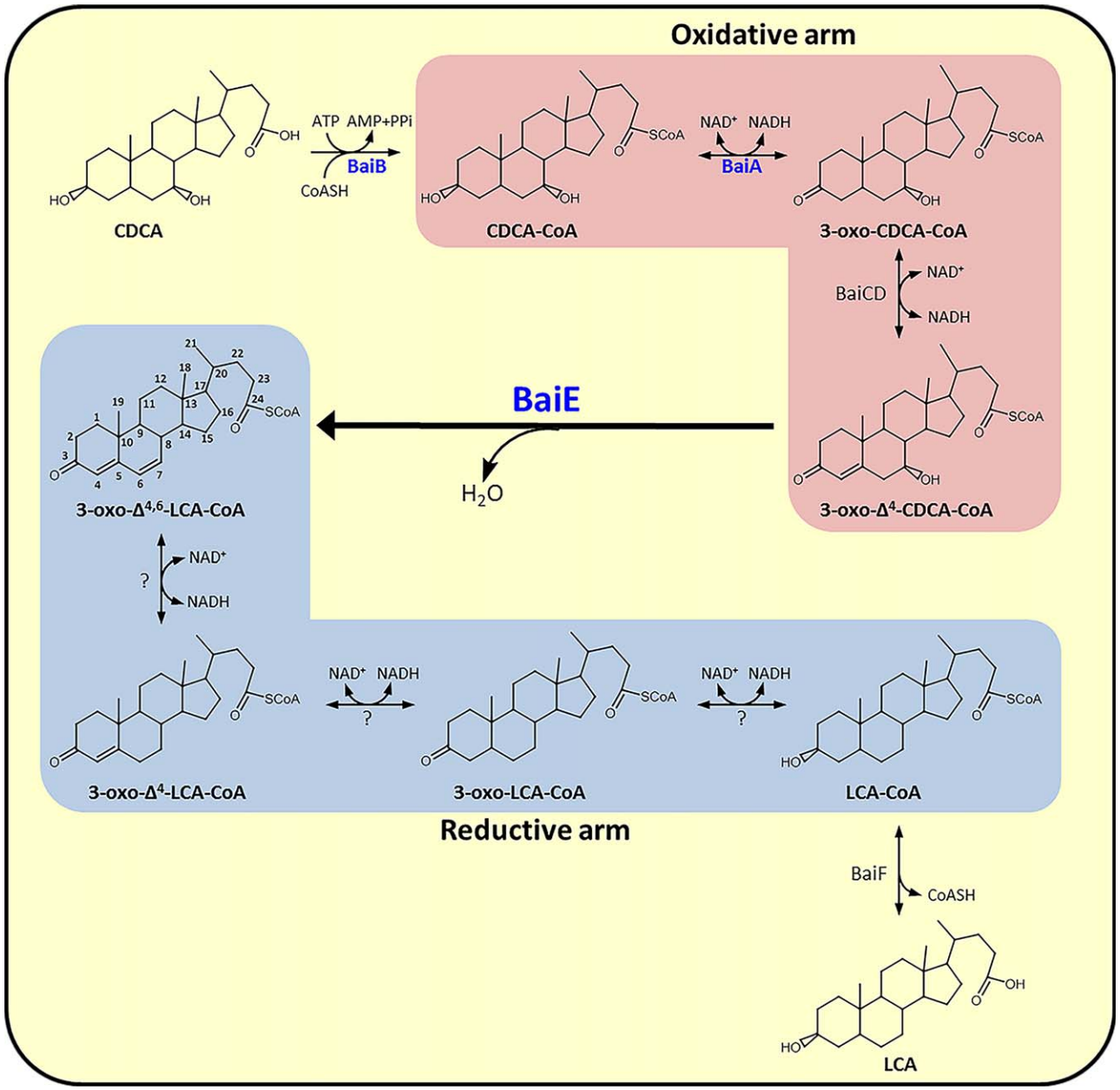

Figure 1

Proposed steps involved in synthesis of secondary bile acid in human gut anaerobe, *Clostridium* sp. The oxidative and reductive arms of the pathway are enclosed within *salmon* and *blue colored boxes*, respectively. Enzymes with crystal structures solved using the JCSG pipeline are denoted in *blue*.

La Jolla, CA). The expression vector pSport1-19k containing the *baiE* sequence was used as a template.[20]

Protein expression and purification

Proteins utilized for structure determination and kinetic studies were prepared as described previously.[22] Briefly, recombinant protein was expressed at 37°C by induction of the arabinose promoter with L-arabinose (0.13%) for 6 h in a 0.5 L culture and purified by single step Ni-NTA chromatography on a 1.5 mL bed volume. LC-MS and SDS-PAGE analysis were consistent with the 22 kDa predicted molecular mass of the BaiE monomer with an N-terminal expression and purification tag. The oligomeric profile was determined by analytical size exclusion chromatography performed at room temperature on an Agilent HP1100 HPLC system utilizing a Shodex 8 × 300 mm Protein KW-802.5 column in 20 m*M*

Tris pH 7.5, 200 m*M* NaCl, 0.5 m*M* TCEP, and 3 m*M* NaN_3. The N-terminal expression and purification tags were not cleaved in this study. Selenomethionine (Se-Met) derivatized proteins were utilized for structure determination and native proteins were utilized for kinetic studies and co-crystallization trials.

Synthesis of bile acid substrates and products

CoA-thioesters of bile acids were prepared as described previously.[22] 3-Oxo-Δ^4-chenodeoxycholic acid (3-oxo-Δ^4-CDCA)[26] and 3-oxo-$\Delta^{4,6}$-lithocholic acid (3-oxo-$\Delta^{4,6}$-LCA)[27] were synthesized following published procedures. Commercially obtained chemicals used in the synthesis were utilized without further purification or drying.

Steady-state kinetics

Steady-state kinetic parameters were determined using a Varian Cary 100 Bio UV–Visible spectrophotometer equipped with a thermo-jacketed cuvette holder. The reactions at 25°C in 20 m*M* Tris–HCl pH 7.3 monitored the formation of the product at 297 nm. Reaction rates were investigated under varying substrate concentrations below and above the respective K_M values. The initial linear regions of the reaction progress curves were utilized for determining the reaction rates. The data were fitted to the Michaelis–Menten equation by non-linear regression method using the enzyme kinetics module in GraphPad Prism (GraphPad Software, La Jolla, CA).

Detection of substrate turnover by ^{1}H-NMR

^{1}H-NMR spectra were acquired at 300°K on a Bruker Avance instrument equipped with a 1H/13C/15N-TXI cryoprobe operating at 600 MHz with 16 scans and a recycle delay of 2 s employing excitation sculpting to suppress water signal (Hwang and Shaka). Isotope-labeled compounds were purchased from Sigma-Aldrich/Isotec. All reaction samples contained 3-(trimethylsilyl)−2,2′,3,3′-tetradeuteropropionic acid as an internal standard that was referenced to 0 ppm and 10% D_2O. The reaction was initiated by adding enzyme to an ice cold solution containing 100 μ*M* substrate prepared in deuterated DMSO. Samples were immediately transferred to the NMR instrument and data collection initiated after temperature equilibration as determined by the stability of the signal.

Substrate binding assay

Purified protein (100 μg) was suspended in 50 μL of reaction mixture containing 25 m*M* sodium acetate pH 7.5 with 3-[N-morpholino]propanesulfonic acid (MOPS) and bile acid substrate (18,000 dpm). The reaction was incubated for 1 min at 37°C in 10K Nanosep centrifugal concentrators (Pall Filtron). The concentrators were centrifuged at 10,000*g* for 2 min. Samples were washed with an additional 100 μL of reaction buffer and centrifuged again for 2 min. Bound counts and effluents were quantified by liquid scintillation spectrometry. Bound counts were corrected for non-specific binding against assays with heat-denatured protein and background binding to the filter.

Crystallization of BaiE

Selenomethionine derivatized BaiE protein from *C. scindens* ATCC35704, and *C. hiranonis* DSM13275 yielded crystals from the JCSG Core Suite (Qiagen Sciences, MD), conditions I-D8 (20% w/v PEG3350, 0.2*M* sodium sulfate, pH 6.6; space group $P3_121$), and IV-D4 (50% w/v PEG200, 0.1*M* HEPES pH 7.5; space group $P6_3$), respectively. Standard JCSG protocols were utilized for all crystallization trials[28,29] using a drop volume of 0.2 μL and a 1:1 (vol/vol) ratio of reservoir to protein (18.6 mg/mL, *C. scindens* ATCC35704 and 20.6 mg/mL *C. hiranonis* DSM13275) in 20 m*M* HEPES pH 8.0 solution equilibrated against 100 μL of reservoir solution. The crystals were cryoprotected with addition of 10% 1,2 ethanediol (*C. scindens* ATCC35704) or 10% glycerol (*C. hiranonis* DSM13275) before harvesting and flash freezing with liquid nitrogen. Co-crystallization trials involving native preparations of the proteins were performed similarly with addition of 1 m*M* product, 3-oxo-$\Delta^{4,6}$-Lithocholyl-Coenzyme A (3-oxo-$\Delta^{4,6}$-LC-CoA). Partial binding of the product (see below) was observed in only one co-crystal of *C. hiranonis* DSM13275 (space group *R32:h*) obtained at a protein concentration of 21 mg/mL from JCSG Core Suite condition I-G5 (10% PEG6000, 0.1*M* citric acid pH 5.0). This crystal was cryoprotected with 15% 1,2-ethanediol. BaiE from *C. hylemonae* DSM15053 (8.5 mg/mL) yielded crystals [JCSG Core Suite condition III-E2 (0.01*M* cobalt chloride, 1.8*M* ammonium sulfate, 0.1*M* MES pH 6.5; space group *R32:h*)], but no ordered binding of the product was observed in the structure. Prior to harvesting, 10% ethanediol was added to the drop.

Structure determination of BaiE

Experimental phases for BaiE homologs from *C. scindens* and *C. hiranonis* were generated by multiple-wavelength anomalous diffraction (MAD) and single-wavelength anomalous diffraction (SAD) methods, respectively. The X-ray diffraction data were collected at wavelengths corresponding to the peak (λ_1), inflection (λ_2), and high-energy remote (λ_3) wavelengths of selenium for the MAD experiments and at the peak wavelength of selenium for the SAD experiments. The data were collected on beamline 11–1 at Stanford Synchrotron Radiation Lightsource at 100 K with a Rayonix Mar Mosaic MX-325 CCD detector using the Blu-Ice data-collection environment.[30] MOSFLM[31] and SCALA[32]

were used for data integrating and scaling. Selenium positions were determined with SHELXD and the phases were refined using autoSHARP,[33] with a mean figure of merit of 0.50–2.9 Å in space group $P3_121$ for *C. scindens* ATCC 35704 and 0.28–1.6 Å in space group $P6_3$ for *C. hiranonis* DSM 13275. Automated model building was performed with ARP/wARP.[34] Data for the crystals grown from the co-crystallization trials were collected on beamline 8.2.2 at the Advanced Light Source with an ADSC Q315 CCD detector at 100 K. The data were reduced with XDS[35] and scaled with XSCALE.[36] The structure of BaiE, *C. hiranonis* DSM13275 was used as a search model for phasing the native BaiE from *C. hylemonae* DSM15053 and BaiE from *C. hiranonis* DSM13275 structures originating from the co-crystallization trials. Model completion and iterative cycles of refinement were performed with COOT[37] and REFMAC[38] from the CCP4 program suite.[39] The TLS refinement protocol included one TLS group per molecule in the asu. Coordinates for 3-oxo-$\Delta^{4,6}$-LC-CoA, polyethylene glycol (PEG) and ethylene glycol were generated using PRODRG.[40] The library files containing the refinement restraints were generated using LIBCHECK within CCP4. The quality of the crystal structure was analyzed using the JCSG Quality Control server (http://smb.slac.stanford.edu/jcsg/QC). This server verifies: the stereochemical quality of the model using AutoDepInputTool,[41] MolProbity,[42] and Phenix,[43] the agreement between the atomic model and the data using RESOLVE,[44] the protein sequence using CLUSTALW,[45] the ADP distribution using Phenix, and differences in R_{cryst}/R_{free}, expected R_{free}/R_{cryst}, and various other items including atom occupancies, consistency of NCS pairs, ligand interactions and special positions using in-house scripts to analyze refinement log file and PDB header. Data collection, model, and refinement statistics are summarized in Table I. Coordinates and the associated structure factors are deposited in the Protein Data Bank (PDB) with following accession codes: 4L8P—BaiE from *C. hiranonis* DSM 13275; 4L8O—BaiE from *C. hylemonae* DSM 15053; 4LEH—*C. scindens* ATCC 35704; 4N3V—BaiE from *C. hiranonis* DSM 13275 with 3-oxo-$\Delta^{4,6}$-LC-CoA.

Docking simulations

Simulated substrate binding was performed with the ASEDOCK module of MOE (Chemical Computing Group, Montreal, Canada) to predict possible enzyme substrate interactions. Models of the substrates 3-oxo-Δ^4-CDCA and 3-oxo-Δ^4-CDC-CoA with expected protonation states were generated using the Molecule Builder of MOE and minimized using the Merck Molecular Force Field 94×. Search for potential substrate-binding pockets were performed with the Site Finder module in MOE using the induced-fit protocol, which allows rotatable bonds during refinement of the docked molecules. The top 30 hits were retained for further analysis for relevance to catalysis.

RESULTS AND DISCUSSION

Structure of BaiE, bile acid 7α-dehydratase

The final BaiE structures contained one (*C. hiranonis* DSM13275 in space group $P6_3$ and *C. hylemonae* DSM 15053 in space group *R32:h*), three (*C. scindens* ATCC 35704 in space group $P3_121$), and two (*C. hiranonis* DSM13275 in space group *R32:h*) monomers in the asymmetric unit with R_{cryst}/R_{free} ranging between 15.1/18.1 and 19.4/22.5, consistent with the respective resolutions (Table I). The apo-structures were superimposed using the Secondary Structure Matching (SSM) function in COOT[46] with pairwise *rmsds* ranging from 0.71 to 0.94 Å [Fig. 2(A)]. The major difference in the structures is in the loop formed by residues 48–63, which is in a significantly distinct conformation in each structure. The electron density for the main chain and side chains is well defined throughout, except for the last two C-terminal residues of *C. hiranonis* DSM13275 and the last three residues of *C. hylemonae* DSM15053. In addition only Gly0 of the N-terminal expression and purification tag had clearly interpretable electron density. All models exhibited high-quality geometry with overall clash scores greater than 99th percentile, and Ramachandran plot with greater than 97% residues in favored regions as calculated by MolProbity (v4.02b-509).[47] The hexagonal crystals of BaiE from *C. hiranonis* DSM13275 diffracted to the highest resolution of 1.60 Å.

The BaiE protomer is a single domain structure bearing the characteristic twisted α + β barrel fold of the NTF2-like protein superfamily.[48] The secondary structure elements consist of three α-helices and six β-strands [Fig. 2(B)]. The six β-strands that form the antiparallel curved β-sheet are assembled on one side of the monomer with a *β2–β1–β6–β5–β4–β3* strand order. The three α-helices flank the other side of the molecule and consist of a 34-residue N-terminal helix, α1, and two α-helices of 5 (α2) and 11 (α3) residues. Inspection of the main-chain B-values indicate that residues 48–63 tend to exhibit the highest values in all structures, suggesting conformational flexibility [Fig. 2(B)]. A previously reported homology model of BaiE from *C. scindens* VPI 12708[15] superposes quite well with the crystal structures with a backbone *rmsd* of 1.7 Å for the core α + β barrel fold; however, as expected notable differences are observed for residues 48–63.

Analytical size exclusion chromatography indicated that all BaiE homologs reported here from trimers in solution. BaiE also assembles as a trimer in the crystal structure [Fig. 2(C)]. The asymmetric unit of the *C. scindens* ATCC35704 BaiE crystal (space group $P3_12$)

Table I
Data Collection and Refinement Statistics

Crystal	*C. hiranonis* DSM 13275		*C. scindens* ATCC 35704		*C. hylemonae* DSM 15053	*C. hiranonis* DSM 13275:3-oxo-$\Delta^{4,6}$-LC-CoA
PDB id	4L8P		4LEH		4L8O	4N3V
Space group	$P6_3$		$P3_121$		R32:h	R32:h
Unit cell lengths (Å)	a = b = 58.9, c = 91.3		a = b = 109.3, c = 118.3		a = b = 53.0, c = 428.6	a = b = 84.3, c = 311.8
Data collection						
Beamline	SSRL BL11-1		SSRL BL11-1		ALS 8.2.2	ALS 8.2.2
Data set	SAD	λ_1 MAD	λ_2 MAD	λ_3 MAD	Native	Native
Wavelength (Å)	0.9795	0.9790	0.9795	0.9184	1.000	1.000
Resolution range (Å)	29.5–1.60	29.6–2.90	29.6–2.98	29.5–2.90	28.6–2.20	47.4–1.89
Highest resolution shell (Å)	1.64–1.60	2.98–2.90	3.06–2.98	2.98–2.90	2.32–2.20	1.94–1.89
No. of observations	172,513	137,535	63,001	68,430	77,498	362,382
No. of unique reflections	23,715	18,559	17,071	18,502	12,340	34,714
Completeness (%)	100 (100)[a]	99.9 (100)	99.9 (100)	99.9 (100)	99.3 (96.0)	99.9 (98.8)
Mean $I/\sigma(I)$	11.1 (2.7)[a]	13.1 (1.8)	11.3 (2.0)	11.2 (1.8)	17.1 (2.7)	19.5 (2.5)
R_{merge} on I (%)[b]	9.5 (65.1)[a]	9.4 (112.3)	7.3 (61.8)	7.1 (73.0)	9.5 (55.7)	6.9 (88.5)
R_{meas} on I (%)[c]	10.2 (70.3)[a]	10.1 (120.6)	8.5 (72.3)	8.3 (85.5)	10.4 (61.9)	7.3 (95.3)
R_{pim} on I (%)[d]	3.8 (26.4)[a]	3.7 (43.5)	4.4 (36.8)	4.2 (43.8)	4.1 (26.4)	2.2 (35.0)
Model and refinement statistics						
Data used in refinement			λ_1 MAD			
No. of reflections (total)[g]	23,680		18,530		11,786	34,711
No. of reflections (test)	1,222		948		568	1,748
Cutoff criteria	|F|>0		|F|>0		|F|>0	|F|>0
R_{cryst} (%)[e]	15.1		17.7		19.4	18.8
R_{free} (%)[f]	18.1		21.7		22.5	21.8
Stereochemical parameters						
Restraints (RMSD observed)						
Bond lengths (Å)	0.011		0.011		0.013	0.010
Bond angles (°)	1.49		1.49		1.32	1.38
MolProbity statistics						
Ramachandran plot (%)[h]	97.6 (0)		98.0 (0)		98.8 (0)	99.4 (0)
Rotamer outliers (%)	2.1		0.7		0.0	2.1
All atom clashscore	1.4		1.0		0.4	3.2
Average isotropic B-value (Å^2)[i]	24.8 (17.7)		96.3 (104.1)		35.2 (39.4)	35.8 (26.2)
ESU based on R_{free} (Å)	0.08		0.31		0.18	0.13
Protein residues/atoms	168/1366		501/4091		168/1335	334/2722
Non-protein entities	124 H_2O, 1 Ni^+, 1 Na^+, 2 PEG fragments		3 H_2O, 8 SO_4^{2-}, 1 Zn^{2+}		70 H_2O, 1 SO_4^{2-}, 1 Co^{2+}, 1 Na^+, 4 ethylene glycol	189 H_2O, 1 UNL, 2 Zn^{2+}, 2 Na^+, 2 citric acid, 1 ethylene glycol, 1 PEG fragment

[a]Values in the parentheses are for the highest resolution shell.
[b]$R_{merge} = \Sigma_{hkl}\Sigma_i|I_i(hkl) - <I(hkl)>|/\Sigma_{hkl}\Sigma_i I_i(hkl)$.
[c]R_{meas}(redundancy-independent R_{merge}) $= \Sigma_{hkl}[N_{hkl}/(N_{hkl}-1)]^{1/2}\Sigma_i|I_i(hkl) - <I(hkl)>|/\Sigma_{hkl}\Sigma_i I_i(hkl)$.
[d]R_{pim}(precision-indicating R_{merge}) $= \Sigma_{hkl}[1/(N_{hkl}-1)]^{1/2}\Sigma_i|I_i(hkl) - <I(hkl)>|/\Sigma_{hkl}\Sigma_i I_i(hkl)$.
[e]$R_{cryst} = \Sigma||F_{obs}| - |F_{calc}||/\Sigma|F_{obs}|$, where F_{calc} and F_{obs} are the calculated and observed structure factor amplitudes, respectively.
[f]R_{free} = as for R_{cryst}, but for 5% of the total reflections chosen at random and omitted from refinement.
[g]Typically, the number of unique reflections used in refinement is slightly less than the total number that were integrated and scaled. Reflections are excluded due to systematic absences, negative intensities and rounding errors in the resolution limits and cell parameters.
[h]Percentage of residues in favored regions (Top8000) of Ramachandran plot (outliers in parenthesis).
[i]This value represents the total B that includes TLS and residual B components. (Wilson plot B-value in parenthesis.).

contains what is assumed to be the biological trimer. Similar trimer assemblies can be generated in the other crystal forms by crystallographic symmetry. The trimer interface primarily involves α1 and strand-swapped interactions between β6 and the C-terminal "strand" of the neighboring monomer that stabilizes the bottom of the trimer, with addition minor contributions from β3, β4. Several key interactions are predicted to stabilize the inter-protomer interactions including an octahedral six-atom coordination of a divalent metal ion at the trimer interface. The metal ion coordinates with three H86-Nϵ2 atoms from each symmetry-related subunit of the trimer and three water molecules within 2.2 Å. This divalent ion–His coordination at the trimer interface is conserved across all known structures of BaiE homologs. The presence of a divalent metal ion at the subunit interface has been previously reported and considered to stabilize the quaternary assembly.[49] The anomalous difference Fourier

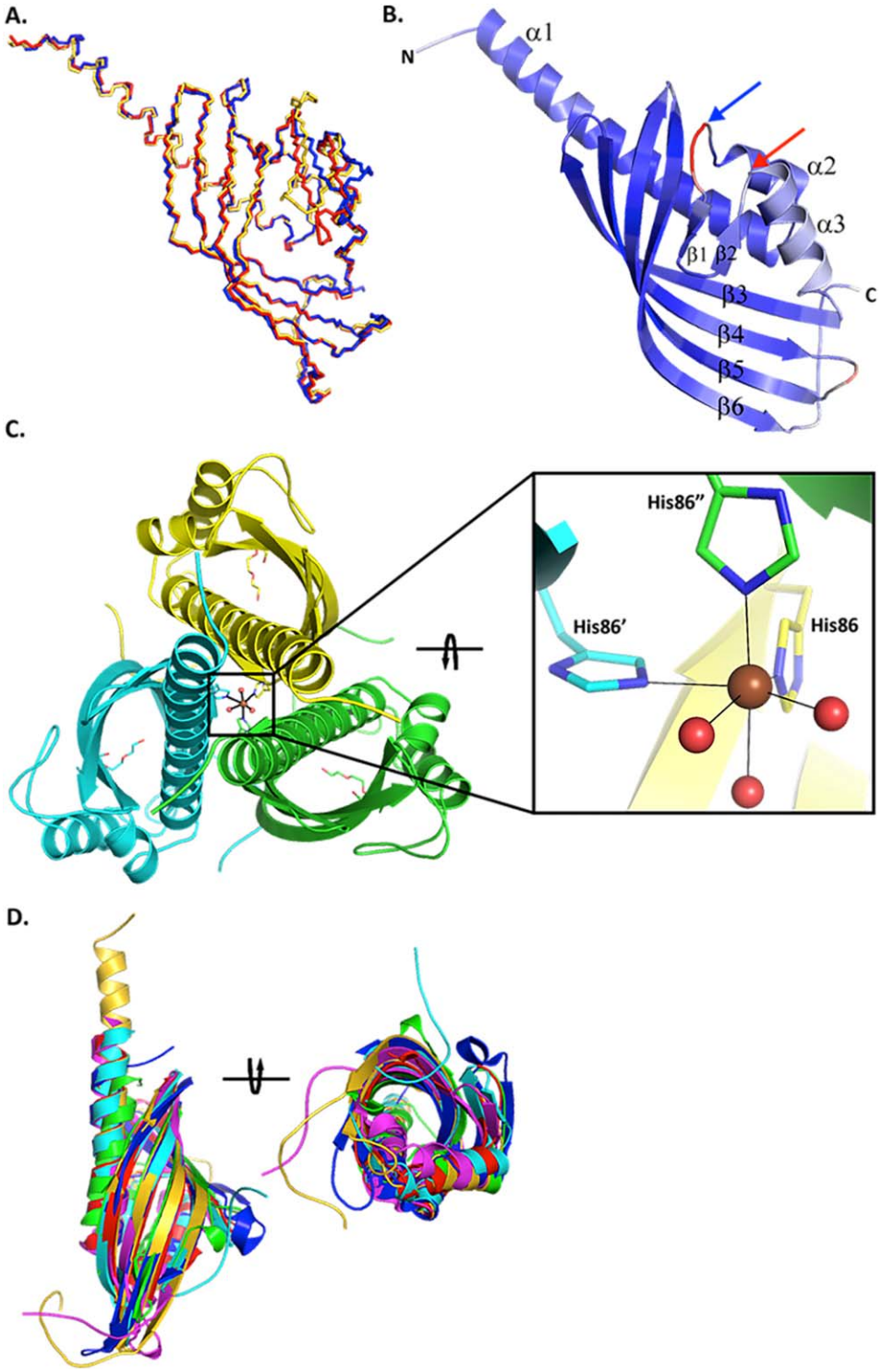

Figure 2

Structure of BaiE, bile acid 7α-dehydratase. (**A**) Secondary structure match (SSM) superposition of BaiE crystal structures from different organisms. The main chain is *colored gold, red,* and *blue,* respectively, for *C. hiranonis* DSM13275, *C. scindens* ATCC35704 and *C. hylemonae* DSM15053. (B) Characteristic twisted α + β barrel fold observed in BaiE. The secondary structure elements are colored according to C^{α} atomic *B*-value from *blue* (lowest *B*-value: 20 $Å^2$) to *red* (highest *B*-value: 65 $Å^2$). The *blue* and *red arrows,* respectively, indicate the start and end of loop residues 48–63. (**C**) Trimer assembly interface as observed in the crystal packing of BaiE, *C. hiranonis* DSM13275. Bound PEG molecules in the active site are indicated as *sticks.* The three subunits of the trimer assembly are colored *yellow, cyan* and *green.* The six atom, $(His)_3$-$(H_2O)_3$, octahedral coordination of the Ni ion is depicted in the square panel. The view in the square panel corresponds to an ∼90° clockwise rotation of the view of the trimer assembly in the primary figure around an axis perpendicular to the three-fold symmetry axis. The coordinate bonds are depicted as *solid black lines.* N, O, and Ni atoms are colored *blue, red,* and *brown,* respectively. The carbon atoms of the protein chain are colored *yellow, cyan,* and *green,* respectively. (**D**) SSM superposition of BaiE, *C. hiranonis* DSM13275 (*gold*), onto closest structural homologues as determined by DALI. The proteins used in the superposition are two scytalone dehydrogenases (*blue* and *cyan*), LinA (*magenta*), an α + β barrel fold containing protein of unknown function (PDB ID: 3ROB), and $\Delta^{5,3}$-ketosteroid isomerase (*green*). Two views between the figures are related by ∼90° anticlockwise rotation.

electron density maps suggests a mixture of Ni^{2+} and Zn^{2+} ions in the trimer interface of BaiE, *C. hiranonis* DSM13275. The Ni^{2+} likely originated from the metal affinity column used for purification, whereas Zn^{2+} was likely acquired during protein production. Neither of these metal ions was present in the purification or crystallization buffers. The peak intensity for Ni^{2+} in the structure is higher than Zn^{2+} as it likely that some Zn may have been exchanged with Ni during purification. Based on these observations, we modeled the divalent metal ion at the trimer interface in the final deposited model of BaiE, *C. hiranonis* DSM13275 as Ni^{2+}. However, the divalent metal ion in the deposited model of the homolog from *C. scindens* ATCC35704 is modeled as Zn^{2+} based on the X-ray fluorescence spectroscopy[50] (data not shown). For the homolog from *C. hylemonae* DSM15053, X-ray fluorescence data were inconclusive and the divalent metal ion was modeled as Co^{2+} since the crystallization reagents contained $CoCl_2$. Many intersubunit salt bridge interactions are also present at the trimer interface (E4–R6, R6–E11, E21–K24, R32–E89, and E150–R154) in addition to multiple hydrogen bond interactions. Similar trimer interface salt bridges and hydrogen bond interaction are also observed in related structures from this protein family, such as scytalone dehydratase (STD)[48] and LinA.[51] However, to our knowledge, the metal–His interaction at the trimer interface in BaiE is the first such interaction observed in this family.

Analysis using DALI[52] and FATCAT[53] suggest BaiE is similar to members of the NTF2 superfamily [Fig. 2(D)] The closest structural homologs are STDs (DALI *Z* score: 16.8) and LinA (DALI *Z* score: 16.1). SSM superposition by COOT achieved a core backbone *rmsd* of 1.5 Å >126 C^{α} atoms for comparison with STD[54] (PDB ID: 3STD), 2.6 Å >110 C^{α} atoms with $\Delta^{5,3}$-ketosteroid isomerase[55] (PDB ID: 1OPY), and 3.2 Å >117 C^{α} atoms with LinA (PDB ID: 3A76). BaiE possesses less than 10% sequence identity with the closest structurally related protein.

Substrate binding site

Analysis of both the monomer and the trimer BaiE structure with the Site Finder module of the Molecular Operating Environment package (MOE; Chemical Computing Group, Montreal, Canada) indicates that the substrate-binding pocket [Fig. 3(A)] is the largest surface cavity with a volume of 451 $Å^3$ as determined by CASTp[56] [Fig. 3(B)]. Secondary structure elements α1, β1, and β2 form the mouth, while α3, β3, β4, β5, and β6 form the floor of the binding pocket. Y30 (α1), D35 (α1), and H83 (β3) that were shown to participate in catalysis by site-directed mutagenesis (see below) are indeed located in the substrate binding pocket. Crystal structures of the four BaiE homologs revealed the D35 and H83 side chains interact within a distance of 2.8 Å [Fig. 3(C)]. However, no interaction is observed between Y30 and the other two catalytic residues. In BaiE, *C. hiranonis* DSM13275, Y30 interacts (2.8 Å) with an oxygen atom of a PEG molecule bound in the active site. D106 (β4) and R146 (β6) in the substrate binding pocket are conserved across all the BaiE homologs and interact via a salt bridge (2.8 Å) that is conserved in all apo-structures of BaiE homologs.

Predicted enzyme:substrate interaction by simulated docking experiments

Docking experiments of the substrate 3-oxo-Δ^4-CDCA into the BaiE binding pocket with the ASEDock module of MOE identified a potentially productive binding mode that is consistent with our site-directed mutagenesis experiments [Fig. 4(A)]. In this binding mode, the *C3*-oxo and *C7*-hydroxyl groups are located 3.1 and 3.6 Å from Y30-Oη and H83-Nε2 atoms, respectively. H83—Nε2 is 2.7 Å from the 6α-hydrogen compared with 4.5 Å from the 6β-hydrogen. The H83–imidazole is therefore positioned to abstract the 6α hydrogen and protonate the leaving *C7*-hydroxy group complying with a *cis*-elimination of water (6αH, 7α-OH). However, previous studies with triply tritiated and singly C^{14} labeled cholic acid (6α, 6β, 8β-H^3, 24-C^{14}) detected a diaxial *trans*-elimination of water (6βH, 7α-OH).[57] Further experiments with purified BaiE utilizing 3-oxo-Δ^4 derivatives of both α- and β-muricholic acid (3α,6β,7α-trihydroxy-5β-cholanoic acid) and hyocholic acid (3α,6α,7α-trihydroxy-5β-cholanoic acid) should help resolve the stereochemistry of the 7α-hydroxyl elimination reaction.

Computational calculations with the substrate 3-oxo-Δ^4-CDC-CoA predicted probable binding interactions of the CoA moiety in addition to predicting a similar productive binding mode of the bile acid moiety [Fig. 4(B)]. The calculation predicted a twisted conformation of CoA where the adenine moiety is involved in a π–π stacking interaction with Y115. In such a conformation, a significant portion of both the pantetheine and AMP moieties of CoA would be exposed to the bulk solvent without any direct interaction with the protein. This scenario has previously been observed in crystal structures of thiolase where the AMP portion projects out of the substrate binding pocket and interacts only with surface residues.[58,59] Thus, it seems that only the bile acid moiety binds in the active site pocket with no space to accommodate the CoA moiety. The CoA moiety likely projects out in the solvent possibly interacting with surface residues. This topology is supported by the co-crystal structure of BaiE with 3-oxo-$\Delta^{4,6}$-LC-CoA where the bile acid moiety is observed to bind in the active site and the CoA moiety extends into the solvent exhibiting poor electron density, as described below.

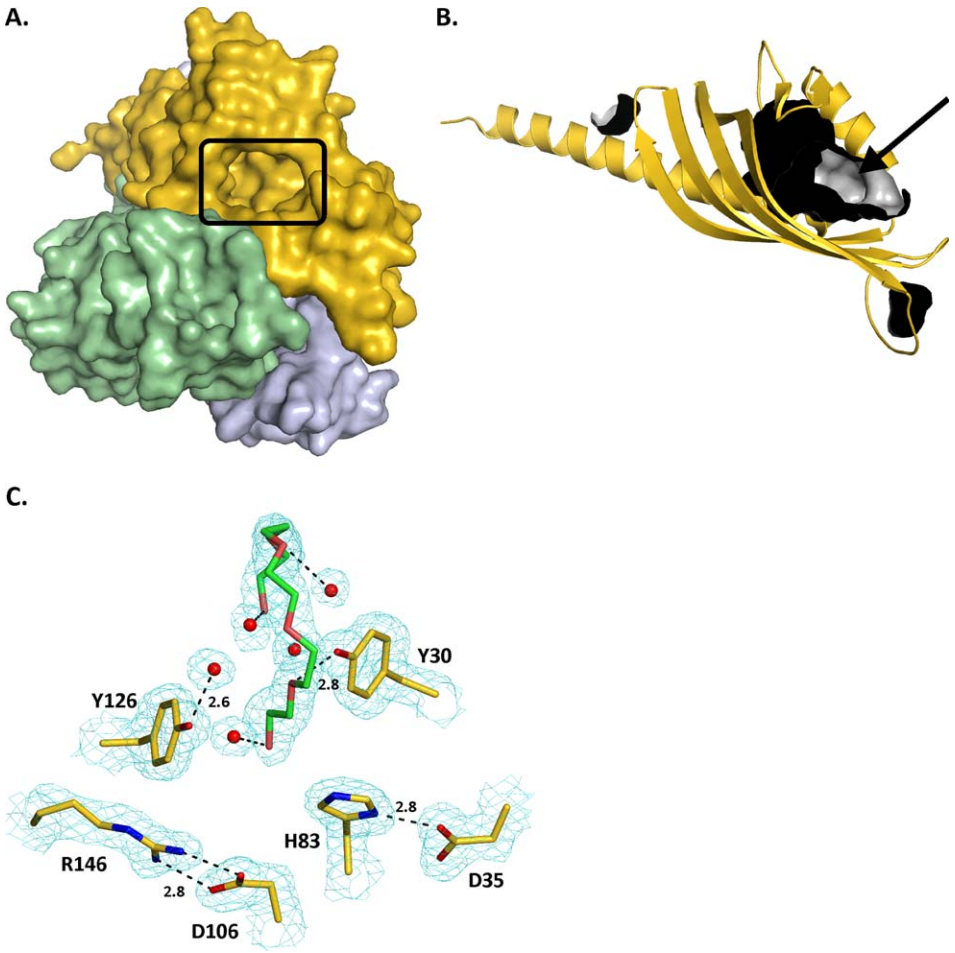

Figure 3

Substrate binding site of BaiE, bile acid 7α-dehydratase. (**A**) Location of the active site of one protomer with respect to the trimer assembly. The protomers of the trimer are colored *gold*, *blue*, and *green*. (**B**) Cavities in the monomer structure of BaiE. Inner surface of the cavities are colored *gray* and the outer surface are colored *black*. The substrate binding site is indicated by the *black arrow*. (**C**) Key interaction involving residues of the substrate binding site with PEG and water molecules in BaiE, *C. hiranonis* DSM13275. *2Fo-Fc* electron density map colored cyan contoured at 1.0 sigma. *Dashed black lines* are hydrogen bond interactions with distances in Å between the interacting atoms. Carbon atoms of protein residues and PEG molecule are colored *gold* and *green*, respectively. O, N, P, and S atoms are in *red*, *blue*, and *orange*, respectively.

Crystal structure of BaiE·3-oxo-$\Delta^{4,6}$-lithocholyl CoA

The co-crystal structure of BaiE with 3-oxo-$\Delta^{4,6}$-LC-CoA shows a novel extended pocket that was not predicted by the simulated docking experiments. This extended pocket is generated by the substrate binding sites of two protomers that originate from two different trimer assemblies related by two-fold non-crystallographic symmetry (NCS). A key loop comprising residues 48–63 in the substrate binding site of each protomer forms the extended pocket [black and blue circles in Fig. 5(A)]. Interestingly, this loop in the co-crystal structure protrudes into the substrate binding site of the protomer related by NCS. This extended conformation is stabilized by hydrogen bond interaction with several residues from the NCS related protomer [Fig. 5(B)]. Importantly, the D56 carboxylate hydrogen bonds with the H83 imidazole in the NCS related protomer, which is one of the three catalytic residues. An additional set of hydrogen bonds is observed with loop residues T52, Y54, S55, and G57, and their respective partners in the binding site of the two-fold related protomer: K114 (with T52), Y115 (with Y54), H151 (with Y54), R146 (with S55), E149 (with S55), and Y70 (with G57).

Although the resolution (1.9 Å) of the structure is reasonably high, the electron density of the ligand is relatively poor compared with the protein. Analysis of the electron density map suggests partial occupancy and a dual conformation of the substrate across the NCS two-fold axis [Fig. 5(C)]. Attempts at modeling the entire product indicated that the ligand extends from the

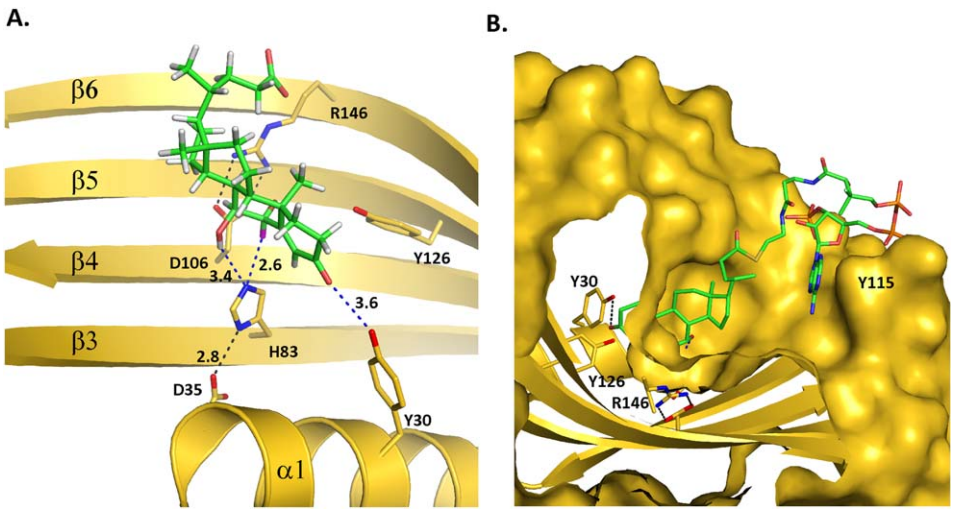

Figure 4

Predicted enzyme:substrate interactions. (**A**) Probable productive binding mode of 3-oxo-Δ^4-Chenodeoxycholate (3-oxo-Δ^4-CDCA). *Blue dashed lines* and distances are predicted interaction of His83-Nϵ2 atom with *C7*-OH and *C6* atoms and Y30-OH group with *C3*-oxo atom of 3-oxo-Δ^4-CDCA. The 6α-H closest to H83-Nϵ2 atom is in *magenta* and 6β-H away from H83–Nϵ2 atom is in *brown*. (**B**) Predicted stacking interaction involving the adenine group of the Coenzyme (CoA) moiety of 3-oxo-Δ^4-Chenodeoxycholyl CoA (3-oxo-Δ^4-CDC-CoA) with Y115. The key interaction of the bile acid moiety of the docked CoA-bile acid ester with the active site residues is similar to what is predicted in (A). Carbon atoms of protein residues and product molecule are in *gold* and *green*, respectively. H, O, N, P, and S atoms are in *gray*, *red*, *blue*, *orange*, and *olive*, respectively.

binding site of one protomer to the binding site of the other protomer with the CoA moiety presumably extending into the solvent. Therefore, the bile acid product was modeled in two different orientations.

As shown in Figure 5(C) in the top and bottom panels, the bile acid moiety is modeled, respectively, into each half of the electron density maps. Furthermore, the ligand comprising only the bile acid and pantetheine moieties fits well into the unbiased *mFo–DFc* electron density at relatively low contour level, +1.8 *rmsd* (0.085 $e^-/Å^3$) in either orientation. In addition, in either orientation, the *C3*-oxo of the bile acid is within 2.7 Å from the side-chain hydroxyl of the active site Y30 within the same protomer. Hence, in the final deposited structure, the bile acid product was modeled in two overlapping orientations in each active site.

The *2mFo–DFc* electron density map generated after addition of the entire product in either orientation revealed continuous electron density features over bile acid moiety and part of the pantetheine moiety at contour levels ranging from +0.8 *rmsd* (0.21 $e^-/Å^3$) to +1.0 *rmsd* (0.26 $e^-/Å^3$). However, the AMP, the dimethyl group, and the pyrophosphate linkage regions do not have electron density coverage. Although an additional electron density blob is observed adjacent to the bile acid moiety, attempts at modeling the AMP moiety into this blob shows that the shape is not consistent with that assignment. Therefore, due to difficulty in unequivocal assignment of the ligand arising from partial occupancy and dual binding mode across the NCS two-fold, the ligand is modeled as an unknown ligand (UNL) with a dual conformation. In the UNL, the AMP moiety, pyrophosphate linkage and dimethyl group are omitted.

Detection of product formation by ^{1}H-NMR

A time series of proton NMR spectra were collected to directly monitor the enzymatic removal of the C7α-hydroxy group and the generation of 3-oxo-$\Delta^{4,6}$ bile acid intermediate by BaiE. These data provided an unambiguous analytical probe to confirm the generated product. Selected regions of proton spectra for the BaiE mediated conversion of 3-oxo-Δ^4-CDC-CoA to 3-oxo-$\Delta^{4,6}$-LC-CoA are shown in Figure 6. Aromatic and methyl regions (left and right panels, respectively) of the spectra acquired at different time points after the addition of enzyme are shown. During the reaction, the intensities of the substrate peaks decrease with a concomitant appearance of a new set of peaks, as readily observed in Figure 6, where the intensity of selected substrate peaks at 5.81, 1.17, and 0.59 ppm (marked with dashed lines) decrease as the reaction proceeds. This intensity loss is associated with the appearance of a new set of peaks at 5.71, 1.05, 0.63 ppm (marked with dotted lines) that increase in intensity. The reaction appeared to be almost complete after 2 hours with only minor evidence of substrate peaks remaining. The chemical shifts of the new peaks perfectly match a control spectrum acquired of 3-oxo-$\Delta^{4,6}$-LC-CoA in the same buffer (compound B in Fig. 6) and is observed for all peaks in the spectra and not isolated only to the regions displayed. Close examination of

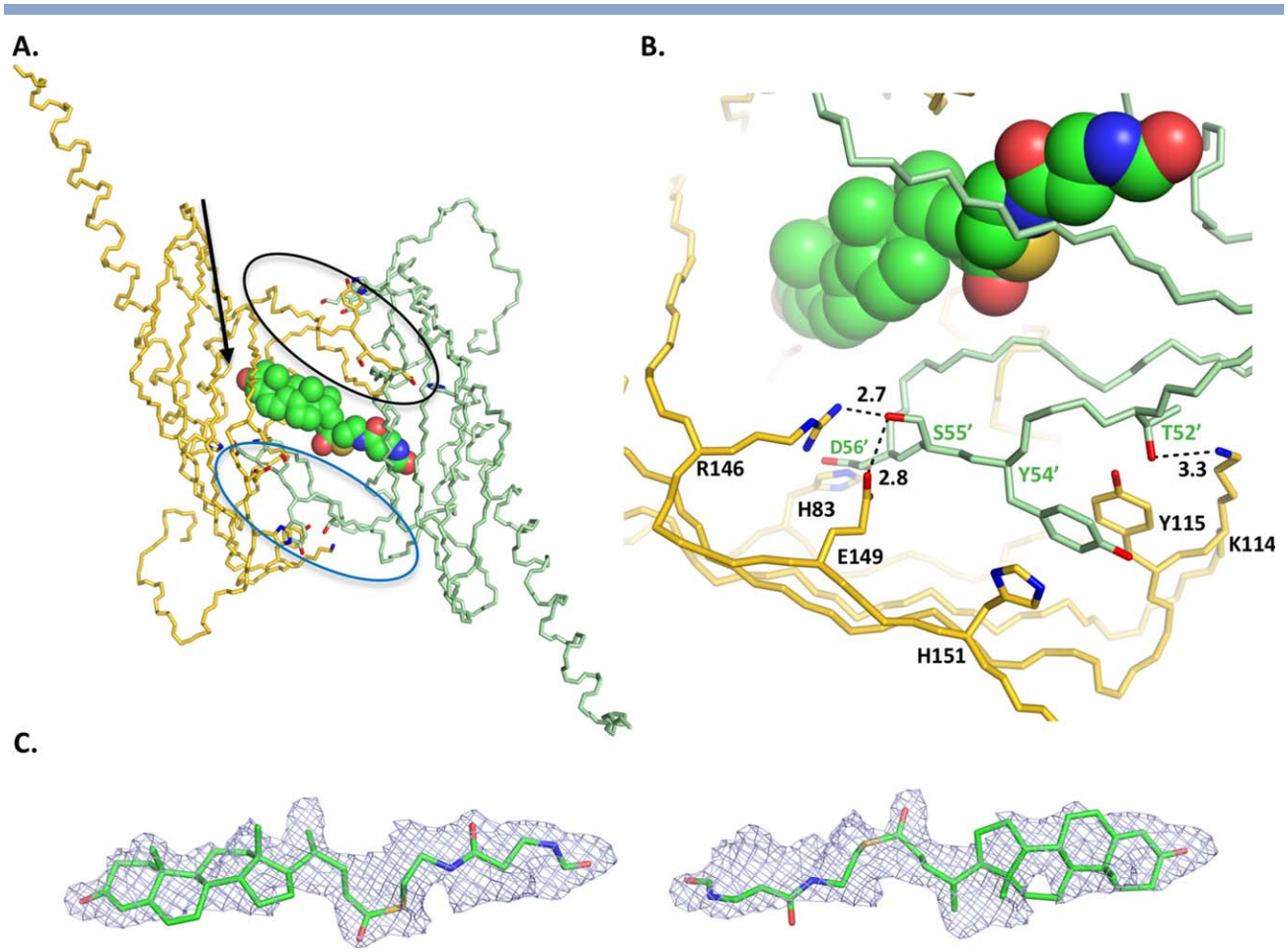

Figure 5

Binding of product, 3-oxo-$\Delta^{4,6}$-Lithocholyl-CoA (3-oxo-$\Delta^{4,6}$-LC-CoA, in BaiE, *C. hiranonis* DSM13275. (**A**) The extended binding pocket and binding of 3-oxo-$\Delta^{4,6}$-LC-CoA, in BaiE, *C. hiranonis* DSM13275. Main chain of protomers arising from different trimer assemblies is in *gold* and *green*, respectively. The loop formed by residues 48–63 is bordered by *black* and *blue ellipses* in the *gold* and *green* monomers, respectively. The *black arrow* indicates the location of the *C3*-oxo atom. (**B**) Key inter-protomer interactions involved in generating the extended binding pocket. Numbers indicate distances in Å. (**C**) Unbiased *mFo-DFc* electron density map of 3-oxo-$\Delta^{4,6}$-LC-CoA contoured at +1.8 σ (0.085 $e^{-}/Å^{3}$). For clarity, both orientations of the ligand are shown separately to illustrate how the model fits the density. A model with the two orientations together at partial occupancy fits the density better than either orientation on its own. The pyrophosphate and AMP moiety of the product is not shown. The density fit for those regions is not as good (see text). Product 3-oxo-$\Delta^{4,6}$-LC-CoA in panels A and B is depicted as *spheres*.

the aromatic region in Figure 6 shows the appearance of two new doublets during the reaction as expected for the methene groups generated by removal of the 7α-hydroxyl group. One doublet is isolated and clearly observed at 6.23 ppm (marked with a dotted line) and the second is observed as part of the overlapped peak at approximately 6.14 ppm. These data confirm that BaiE is converting 3-oxo-Δ^{4}-CDC-CoA to the expected product 3-oxo-$\Delta^{4,6}$-LC-CoA.

Site-directed mutagenesis

Mutation of predicted key catalytic and substrate binding residues of BaiE from *C. scindens* VPI 12708 provide important insights into their involvement in substrate turnover and binding (Table II). Y30F, D35N, and H83N mutations completely abolished substrate turnover indicating involvement of these residues in catalysis. However, increased substrate binding is observed for mutants Y30F (5.6-fold) and D35N (3.0-fold) compared with wild type, but no substrate binding is found for the H83N mutant. Y30 of BaiE is equivalent to Y14 in 3-oxo-Δ^{5}-ketosteroid isomerase (KSI) and is predicted to participate as a general acid protonating or forming a low barrier hydrogen bond (LBHB) with the dienolate intermediate during the isomerization reaction.[55] Y126 may stabilize the negative charge on the dienolate intermediate as confirmed by 98% reduced catalytic activity observed in Y126F. In KSI, D99 participates in catalysis in a similar manner. H83 and D35 are equivalent to the

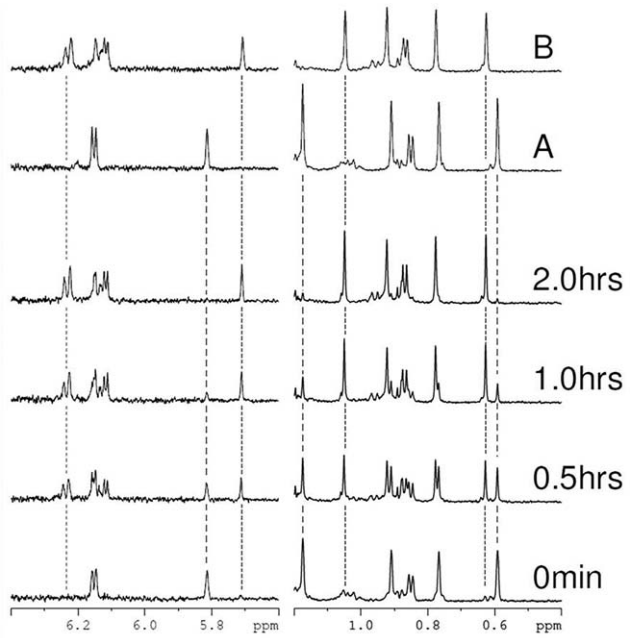

Figure 6

In vitro generation of 3-oxo-$\Delta^{4,6}$- lithocholyl-Coenzyme A from 3-oxo-Δ^4-Chenodeoxycholyl CoA(3-oxo-Δ^4-CDC-CoA) using purified BaiE from *C. hiranonis* DSM13275 as monitored by ^{1}H-NMR. A reaction mixture of 100 μ*M* 3-oxo-Δ^4-CDC-CoA (3-oxo-$\Delta^{4,6}$-LC-CoA) and 0.001 μ*M* BaiE was prepared in 20 m*M* HEPES pH 7.4 and incubated at 300K. Selected regions from one-dimensional ^{1}H-NMR spectra that were acquired at the indicated times after mixing and temperature equilibration (bottom four spectra) are displayed. Reference spectra of 3-oxo-Δ^4-CDC-CoA and 3-oxo-$\Delta^{4,6}$-LC-CoA acquired in the same buffer are shown at the top labeled **A** and **B**, respectively. Some representative peaks associated with 3-oxo-Δ^4-CDC-CoA and 3-oxo-$\Delta^{4,6}$-LC-CoA are marked with *dashed* and *dotted lines*, respectively. The intensity of peaks associated with the substrate decrease with a concomitant increase in product peaks during the reaction. The spectrum of the product matches perfectly the spectra of 3-oxo-$\Delta^{4,6}$-LC-CoA. Examination of the amide region of the spectra (right hand panel) shows the appearance of two new peaks during the reaction and is associated with removal of the 7α-hydroxyl group and the generation of methene groups.

H85–D31 catalytic dyad in STD that is predicted to participate as a general base.[60] Mutation of the H85–D31 pair in STD also impaired catalysis. Site-directed mutagenesis also revealed D106 and R146 in the substrate binding pocket as essential for catalysis. In all apo-structures of BaiE, side chains of D106 and R146 interact via salt bridge at a distance of 2.9 Å. Disruption of this salt bridge by mutation to Asn and Gln at positions 106 and 146, respectively, abolished catalysis.

Site-directed mutagenesis of one residue of the conformationally flexible loop comprising residues 48–63 indicates the importance of this loop in catalysis. A Y54F mutation reduced enzyme activity by 74% compared with wild type, whereas Y54A abolished enzyme activity. This result suggests Y54 is probably important for maintaining the shape of the active site and recognition of the substrate. In the 3-oxo-$\Delta^{4,6}$-LC-CoA co-crystal structure of BaiE, Y54 seems to be involved in key stacking interactions with Y115 and H151 of the NCS two-fold related monomer at the pocket interface.

Table II
Relative Activity and Substrate Binding of Several Site-Directed Mutants of BaiE, *C. scindens* VPI12708

BaiE mutation	Relative activity[a]	Substrate binding (%)
Wild type	+++	1.5
Y30F	–	8.4
D35N	–	4.6
Y54A	–	2.8
Y54F	++	4.1
H83N	–	<0.1
D106N	–	2.3
Y126F	+	10.7
R146Q	–	10.4

[a]Dash denotes activity assays where <0.1% of substrate converted to product.

Steady state kinetic studies

Steady-state kinetics (Table III) analysis was performed by continuous UV assay monitoring of the formation of product utilizing an extinction coefficient, $\varepsilon_{297} = 0.0188/\mu M/cm$, measured at pH 7.3. All four homologs of BaiE revealed robust turnover of CoA-esters of bile acid and free bile acid substrates. The substrate affinity, K_M, for

Table III
Steady State Kinetic Parameters of Different Homologs of BaiE from Key *Clostridium* sp. Associated with Secondary Bile Acid Synthesis[a]

Homolog	Kinetic parameters	Substrates	
		3-oxo-Δ^4-CDCA	3-oxo-Δ^4-CDC-CoA
BaiE_15053	k_{cat} (sec^{-1})	18.6 (0.6)	12.6 (0.6)
	K_M (μ*M*)	21.0 (2.0)	11.4 (1.9)
	k_{cat}/K_M (μM^{-1} sec^{-1})	0.9	1.1
BaiE_13275	k_{cat} (sec^{-1})	4.4 (0.1)	22.2 (2.6)
	K_M (μ*M*)	25.0 (1.8)	208.0 (40.0)
	k_{cat}/K_M (μM^{-1} sec^{-1})	0.2	0.1
BaiE_35704	k_{cat} (sec^{-1})	18.0 (0.9)	15.0 (0.2)
	K_M (μ*M*)	11.0 (1.9)	1.2 (0.2)
	k_{cat}/K_M (μM^{-1} sec^{-1})	1.6	12.5
BaiE_12708	k_{cat} (sec^{-1})	24.0 (1.4)	98.0 (2.7)
	K_M (μ*M*)	9.9 (2.1)	4.0 (0.56)
	k_{cat}/K_M (μM^{-1} sec^{-1})	2.4	24.5

[a]Steady state kinetic parameters were analyzed at substrate concentrations ranging beyond and below the respective K_M values. Reaction was monitored by the formation of product 3-oxo-$\Delta^{4,6}$-lithocholic acid and 3-oxo-$\Delta^{4,6}$-lithocholyl-CoA for respective substrates at wavelength 297 nm. Values in parentheses indicate standard error.
BaiE_15053: BaiE from *Clostridium hylemonae* DSM15053.
BaiE_13275: BaiE from *Clostridium hiranonis* DSM13275.
BaiE_35704: BaiE from *Clostridium scindens* ATCC35704.
BaiE_12708: BaiE from *Clostridium scindens* VPI12708.

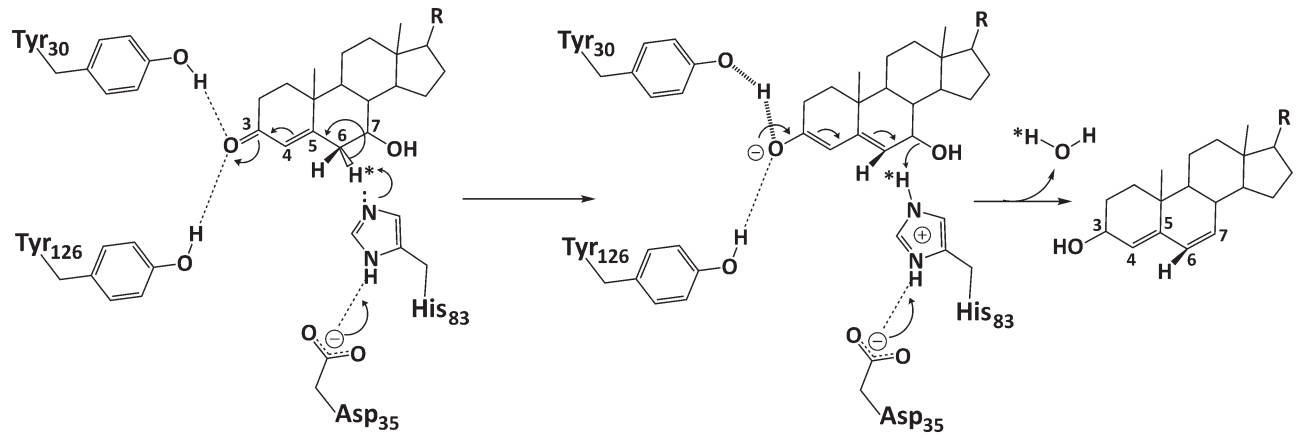

Figure 7

Proposed mechanism of catalysis by BaiE highlighting the role of catalytically important residues in elimination of the 7α-hydroxy group through release of a water molecule.

the free bile acid substrate, 3-oxo-Δ^4-CDCA is of comparable magnitude across all the four homologs. The K_M values of the CoA-bile acid ester 3-oxo-Δ^4-CDC-CoA are also of comparable magnitude across all homologs except for BaiE *C. hiranonis* DSM13275 where the K_M is 208 μ*M*, which is at most two orders of magnitude higher than the others. Furthermore, the turnover rate constants (k_{cat}) of both substrates are comparable in all three homologs except *C. scindens* VPI12708, where the k_{cat} is at most 7.7 times higher. Both BaiE homologs from *C. scindens* ATCC35704 and VPI12708 respectively exhibited higher substrate specificity (k_{cat}/K_M) toward the CoA-ester substrate by an order of a magnitude. In contrast, both BaiE homologs from *C. hylemonae* DSM15053 and *C. hiranonis* DSM13275, respectively, exhibited k_{cat}/K_M values of equal magnitude toward both substrates. Overall, higher k_{cat}/K_M values are attained for the BaiE homologs from *C. scindens* strains in comparison to the homologs from the other two strains.

Mechanism of catalysis

Based on the active site architecture as observed in the crystal structures and the site-directed mutagenesis study, we propose the following mechanism of catalysis by BaiE (Fig. 7). Y30 acts as a general acid (assisted by Y126) facilitating delocalization of the π-electrons across atoms *C3*, *C4*, *C5*, and *C6*. Based on the 3-oxo-Δ^4-CDC-CoA co-crystal structure, the terminal hydroxyl group of Y30 could potentially protonate the oxyanion generated on *C3*-oxo group to stabilize the negative charge. This would result in an electron shift destabilizing the C6-6αH bond. H83 is then positioned to abstract the 6αH atom and protonate the leaving *C7*α-hydroxy group. D35 maintains the pK_a value of the H83-imidazole group for executing the deprotonation and ensuing protonation reaction with the subsequent release of a water molecule.

CONCLUSION

Combined structural and biochemical analysis of BaiE provides key insights into substrate binding and turnover. The 1.9 Å resolution 3-oxo-$\Delta^{4,6}$-LC-CoA co- crystal structure of BaiE revealed an extended pocket between monomers from different trimer assemblies, although the biological relevance of this is unclear. Substrate and co-factor induced oligomerization is previously noted to be involved in catalysis of varied enzyme classes.[58–61] Moreover, using analytical size exclusion chromatography (AnSEC) on the batch of BaiE *C. hiranonis* DSM13275 that yielded the co-crystal structure, we were able to detect higher-order species of the protein in presence of both bile acid substrates and products (data not shown). Although we have not been able to directly correlate these higher-order species with enzymatic activity, our data suggest possible substrate and ligand-induced oligomerization where the substrate/product binds in the extended pocket created between trimers by conformational flexibility of residues 48–63, as observed in the crystal structure. Comparison of the apo-structures across varied homologs reveals a dramatically different conformation of loop 48–63. The conformational flexibility of this loop at the substrate binding site may be essential for substrate binding. Site-directed mutagenesis studies with Y54F and Y54A mutants of BaiE from *C. hylemonae* VPI12708 revealed respective impaired substrate binding and catalytic activity, suggesting the importance of this loop in catalysis.

The biochemical characterization reported herein provides key insights into the mechanism of catalysis of the enzyme, and also sheds new light onto the pathway.

Steady-state kinetic studies reveal that all homologues of BaiE efficiently turnover both 3-oxo-Δ^4-bile acid and CoA-3-oxo-Δ^4-bile acid esters. This result is in stark contrast to our earlier reported characterization of BaiA enzymes that exhibited substantially high substrate specificity toward CoA-bile acid esters.[22] The substrate selectivity of bile acids is substantially lower for BaiA enzymes. It is unclear at what point in the pathway the CoA moiety is released. Since the BaiE homologues turnover bile acid and CoA-bile acid ester with comparable efficiency, it seems likely that a dual possibility exists in the pathway where the CoA moiety can be removed either before or after elimination of the *C7*-hydroxy group. Strains of human bile acid 7 α/β-dehydroxylating bacteria do not 7-dehydroxylate muricholic acids. This could be due to lack of uptake of muricholic acids (transporter specificity), or ligation to CoA, oxidation of 3-α-hydroxy group, or introduction of a C═C double bond (C4─C5). In other words, the initial reactions in the pathway may not allow the 3-oxo-delata 4–6-β, 7α-dihydroxy-cholenoic acid to be formed. Therefore, it is unclear if the bile acid 7α-dehydratase would recognize this as a substrate. However, muricholic acids are not found in humans and we have been unable to isolate bile acid 7-dehydroxylating bacteria from mice using the same techniques used to successfully isolate these bacteria from human feces. Furthermore, the DNA probes used to detect genes in human isolates give negative results using mice fecal samples. Evaluating the substrate specificity of yet-to-be identified enzymes in the reductive arm of the pathway for CoA-bile acid esters and bile acid is required to understand the role of CoA in the pathway. Site-directed mutagenesis with the homologue from *C. scindens* VPI12708 provides key insights into substrate binding and catalysis. Y30, D35, and H83, which are conserved in the family, were confirmed as active site residues participating in catalysis. In addition, Y54, D106, and R146 in the active site are crucial in catalysis, although they do not directly participate in the catalytic chemistry.

This study has therefore provided key insights into the mechanism of *C7*α-hydroxy group removal from the bile acid moiety catalyzed by BaiE. Previous studies alluded to the possibility of *trans*-elimination as the stereochemical route of the reaction.[57] However, from the crystal structures and simulated docking study, *cis*-elimination is a likely possibility. Further experiments involving 3-oxo-Δ^4 intermediate of α-muricholic acid may ascertain the stereochemical route.

The reaction catalyzed by BaiE is pivotal in the pathway as it catalyzes the only irreversible reaction whereby the intermediate is channeled onto the reductive arm generating the secondary bile acids. Hence, the biochemical and the structural characterization of this enzyme will be crucial in generating key modulators controlling the level of secondary bile acids in disease.

ACKNOWLEDGMENTS

We thank the members of the JCSG high-throughput structural biology pipeline for their contribution to this work. Portions of this research were carried out at the Stanford Synchrotron Radiation Lightsource (SSRL) and the Advanced Light Source (ALS). Use of the Stanford Synchrotron Radiation Lightsource, SLAC National Accelerator Laboratory, is supported by the U.S. Department of Energy, Office of Science, Office of Basic Energy Sciences under Contract No. DE-AC02-76SF00515. The SSRL Structural Molecular Biology Program is supported by the DOE Office of Biological and Environmental Research, and by the National Institutes of Health, National Institute of General Medical Sciences (including P41GM103393). The ALS is supported by the Director, Office of Science, Office of Basic Energy Sciences, Materials Sciences Division of the US Department of Energy under Contract No. DE-AC02-05CH11231 at Lawrence Berkeley National Laboratory. The Berkeley Center for Structural Biology is supported in part by NIH, NIGMS and the Howard Hughes Medical Institute. The contents of this publication are solely the responsibility of the authors and do not necessarily represent the official views of the NIGMS or the NIH.

REFERENCES

1. Sonnenburg JL, Xu J, Leip DD, Chen C-H, Westover BP, Weatherford J, Buhler JD, Gordon JI. Glycan foraging in vivo by an intestine-adapted bacterial symbiont. Science 2005;307:1955–1959.
2. Olszak T, An D, Zeissig S, Vera MP, Richter J, Franke A, Glickman JN, Siebert R, Baron RM, Kasper DL, Blumberg RS. Microbial exposure during early life has persistent effects on natural killer T cell function. Science 2012;336:489–493.
3. Ley RE, Turnbaugh PJ, Klein S, Gordon JI. Microbial ecology: human gut microbes associated with obesity. Nature 2006;444:1022–1023.
4. Frank DN, St. Amand AL, Feldman RA, Boedeker EC, Harpaz N, Pace NR. Molecular-phylogenetic characterization of microbial community imbalances in human inflammatory bowel diseases. Proc Natl Acad Sci USA 2007;104:13780–13785.
5. Lupton JR. Microbial degradation products influence colon cancer risk: the butyrate controversy. J Nutr 2004;134:479–482.
6. Wikoff WR, Anfora AT, Liu J, Schultz PG, Lesley SA, Peters EC, Siuzdak G. Metabolomics analysis reveals large effects of gut microflora on mammalian blood metabolites. Proc Natl Acad Sci USA 2009;106:3698–3703.
7. Wang Y, Holmes E, Nicholson JK, Cloarec O, Chollet J, Tanner M, Singer BH, Utzinger J. Metabonomic investigations in mice infected with *Schistosoma mansoni*: an approach for biomarker identification. Proc Natl Acad Sci USA 2004;101:12676–12681.
8. Yap IKS, Li JV, Saric J, Martin F-P, Davies H, Wang Y, Wilson ID, Nicholson JK, Utzinger JRJr, Marchesi Holmes E. Metabonomic and microbiological analysis of the dynamic effect of vancomycin-induced gut microbiota modification in the mouse. J Proteome Res 2008;7:3718–3728.
9. Hylemon PB, Zhou H, Pandak WM, Ren S, Gil G, Dent P. Bile acids as regulatory molecules. J Lipid Res 2009;50:1509–1520.
10. Thomas C, Pellicciari R, Pruzanski M, Auwerx J, Schoonjans K. Targeting bile-acid signalling for metabolic diseases. Nat Rev Drug Discov 2008;7:678–693.

11. Bernstein H, Bernstein C, Payne CM, Dvorakova K, Garewal H. Bile acids as carcinogens in human gastrointestinal cancers. Mutat Res/Rev Mutat Res 2005;589:47–65.
12. Berr F, Kullak-Ublick GA, Paumgartner G, Munzing W, Hylemon PB. 7 α-dehydroxylating bacteria enhance deoxycholic acid input and cholesterol saturation of bile in patients with gallstones. Gastroenterology 1996;111:1611–1620.
13. Yoshimoto S, Loo TM, Atarashi K, Kanda H, Sato S, Oyadomari S, Iwakura Y, Oshima K, Morita H, Hattori M, Honda K, Ishikawa Y, Hara E, Ohtani N. Obesity-induced gut microbial metabolite promotes liver cancer through senescence secretome. Nature 2013;499:97–101.
14. de Aguiar Vallim TQ, Tarling EJ, Edwards PA. Pleiotropic roles of bile acids in metabolism. Cell Metab 2013;17:657–669.
15. Ridlon JM, Kang D-J, Hylemon PB. Bile salt biotransformations by human intestinal bacteria. J Lipid Res 2006;47:241–259.
16. Mallonee DH, Hylemon PB. Sequencing and expression of a gene encoding a bile acid transporter from *Eubacterium* sp. strain VPI 12708. J Bacteriol 1996;178:7053–7058.
17. Mallonee DH, Adams JL, Hylemon PB. The bile acid-inducible *baiB* gene from *Eubacterium* sp. strain VPI 12708 encodes a bile acid-coenzyme A ligase. J Bacteriol 1992;174:2065–2071.
18. Mallonee DH, Lijewski MA, Hylemon PB. Expression in Escherichia coli and characterization of a bile acid-inducible 3α-hydroxysteroid dehydrogenase from *Eubacterium* sp. strain VPI 12708. Curr Microbiol 1995;30:259–263.
19. Kang D-J, Ridlon JM, Moore IDR, Barnes S, Hylemon PB. *Clostridium scindens baiCD* and *baiH* genes encode stereo-specific 7α/7β-hydroxy-3-oxo-Δ^4-cholenoic acid oxidoreductases. Biochim Biophys Acta 2008;1781:16–25.
20. Dawson JA, Mallonee DH, Björkhem I, Hylemon PB. Expression and characterization of a C_{24} bile acid 7 α-dehydratase from *Eubacterium* sp. strain VPI 12708 in *Escherichia coli*. J Lipid Res 1996;37:1258–1267.
21. Ridlon JM, Hylemon PB. Identification and characterization of two bile acid coenzyme A transferases from *Clostridium scindens*, a bile acid 7α-dehydroxylating intestinal bacterium. J Lipid Res 2012;53:66–76.
22. Bhowmik S, Jones DH, Chiu HP, Park IH, Chiu HJ, Axelrod HL, Farr CL, Tien HJ, Agarwalla S, Lesley SA. Structural and functional characterization of BaiA, an enzyme involved in secondary bile acid synthesis in human gut microbe. Proteins 2013;82:216–229.
23. Klock HE, Koesema EJ, Knuth MW, Lesley SA. Combining the polymerase incomplete primer extension method for cloning and mutagenesis with microscreening to accelerate structural genomics efforts. Proteins 2008;71:982–994.
24. Klock HE, Lesley SA. The Polymerase Incomplete Primer Extension (PIPE) method applied to high-throughput cloning and site-directed mutagenesis. Methods Mol Biol 2009;498:91–103.
25. Mallonee DH, White WB, Hylemon PB. Cloning and sequencing of a bile acid-inducible operon from *Eubacterium* sp. strain VPI 12708. J Bacteriol 1990;172:7011–7019.
26. Iida T, Momose T, Nambara T, Chang FC. Potential bile acid metabolites. X.: syntheses of stereoisomeric 3, 7-dihydroxy-5α-cholanic acids. Chem Pharm Bull (Tokyo) 1986;34:1929–1933.
27. Leppik RA. Improved synthesis of 3-keto, 4-ene-3-keto, and 4,6-diene-3-keto bile acids. Steroids 1983;41:475–484.
28. Elsliger M-A, Deacon AM, Godzik A, Lesley SA, Wooley J, Wüthrich K, Wilson IA. The JCSG high-throughput structural biology pipeline. Acta Crystallogr Sect F Struct Biol Cryst Commun 2010;66:1137–1142.
29. Santarsiero BD, Yegian DT, Lee CC, Spraggon G, Gu J, Scheibe D, Uber DC, Cornell EW, Nordmeyer RA, Kolbe WF, Jin J, Jones AL, Jaklevic JM, Schultz PG, Stevens RC. An approach to rapid protein crystallization using nanodroplets. J Appl Crystallogr 2002;35:278–281.
30. McPhillips TM, McPhillips SE, Chiu H-J, Cohen AE, Deacon AM, Ellis PJ, Garman E, Gonzalez A, Sauter NK, Phizackerley RP, Soltis SM, Kuhn P. Blu-Ice and the Distributed Control System: software for data acquisition and instrument control at macromolecular crystallography beamlines. J Synchrotron Radiat 2002;9:401–406.
31. Leslie AW, Powell H. Processing diffraction data with mosflm. In: Read R, Sussman J, editors. Evolving methods for macromolecular crystallography. Volume245, NATO Science Series. Netherlands: Springer; 2007. pp 41–51.
32. Evans P. Scaling and assessment of data quality. Acta Crystallogr Sect D 2006;62:72–82.
33. Vonrhein C, Blanc E, Roversi P, Bricogne G. Automated structure solution with autoSHARP. Methods Mol Biol 2007;364:215–230.
34. Cohen SX, Morris RJ, Fernandez FJ, Ben Jelloul M, Kakaris M, Parthasarathy V, Lamzin VS, Kleywegt GJ, Perrakis A. Towards complete validated models in the next generation of ARP/wARP. Acta Crystallogr D Biol Crystallogr 2004;60:2222–2229.
35. Kabsch W. XDS. Acta Crystallogr D Biol Crystallogr 2010;66:125–132.
36. Kabsch W. Integration, scaling, space-group assignment and post-refinement. Acta Crystallogr D Biol Crystallogr 2010;66:133–144.
37. Emsley P, Lohkamp B, Scott WG, Cowtan K. Features and development of Coot. Acta Crystallogr Sect D 2010;66:486–501.
38. Murshudov GN, Vagin AA, Dodson EJ. Refinement of macromolecular structures by the maximum-likelihood method. Acta Crystallogr D Biol Crystallogr 1997;53:240–255.
39. Winn MD, Ballard CC, Cowtan KD, Dodson EJ, Emsley P, Evans PR, Keegan RM, Krissinel EB, Leslie AGW, McCoy A, McNicholas SJ, Murshudov GN, Pannu NS, Potterton EA, Powell HR, Read RJ, Vagin A, Wilson KS. Overview of the CCP4 suite and current developments. Acta Crystallogr D Biol Crystallogr 2011;67:235–242.
40. Schuttelkopf AW, van Aalten DMF. PRODRG: a tool for high-throughput crystallography of protein-ligand complexes. Acta Crystallogr D Biol Crystallogr 2004;60:1355–1363.
41. Yang H, Guranovic V, Dutta S, Feng Z, Berman HM, Westbrook JD. Automated and accurate deposition of structures solved by X-ray diffraction to the Protein Data Bank. Acta Crystallogr D Biol Crystallogr 2004;60:1833–1839.
42. Davis IW, Leaver-Fay A, Chen VB, Block JN, Kapral GJ, Wang X, Murray LW, Arendall WB, 3rd, Snoeyink J, Richardson JS, Richardson DC. MolProbity: all-atom contacts and structure validation for proteins and nucleic acids. Nucleic Acids Res 2007;35:W375–383.
43. Adams PD, Afonine PV, Bunkoczi G, Chen VB, Davis IW, Echols N, Headd JJ, Hung LW, Kapral GJ, Grosse-Kunstleve RW, McCoy AJ, Moriarty NW, Oeffner R, Read RJ, Richardson DC, Richardson JS, Terwilliger TC, Zwart PH. PHENIX: a comprehensive Python-based system for macromolecular structure solution. Acta Crystallogr D Biol Crystallogr 2010;66:213–221.
44. Terwilliger TC. Maximum-likelihood density modification. Acta Crystallogr D Biol Crystallogr 2000;56:965–972.
45. Larkin MA, Blackshields G, Brown NP, Chenna R, McGettigan PA, McWilliam H, Valentin F, Wallace IM, Wilm A, Lopez R, Thompson JD, Gibson TJ, Higgins DG. Clustal W and Clustal X version 2.0. Bioinformatics 2007;23:2947–2948.
46. Emsley P, Cowtan K. Coot: model-building tools for molecular graphics. Acta Crystallogr D Biol Crystallogr 2004;60:2126–2132.
47. Davis IW, Murray LW, Richardson JS, Richardson DC. MolProbity: structure validation and all-atom contact analysis for nucleic acids and their complexes. Nucleic Acids Res 2004;32:W615–W619.
48. Lundqvist T, Rice J, Hodge CN, Basarab GS, Pierce J, Lindqvist Y. Crystal structure of scytalone dehydratase — a disease determinant of the rice pathogen, *Magnaporthe grisea*. Structure 1994;2:937–944.
49. Auld D. Zinc coordination sphere in biochemical zinc sites. Biometals 2001;14:271–313.
50. Bearden JA. XRay wavelengths. Rev Mod Phys 1967;39:78–124.
51. Okai M, Kubota K, Fukuda M, Nagata Y, Nagata K, Tanokura M. Crystal structure of γ-hexachlorocyclohexane dehydrochlorinase

LinA from *Sphingobium japonicum* UT26. J Mol Biol 2010;403: 260–269.
52. Holm L, Rosenström P. Dali server: conservation mapping in 3D. Nucleic Acids Res 2010;38:W545–W549.
53. Li Z, Ye Y, Godzik A. Flexible structural neighborhood—a database of protein structural similarities and alignments. Nucleic Acids Res 2006;34:D277–D280.
54. Chen JM, Xu SL, Wawrzak Z, Basarab GS, Jordan DB. Structure-based design of potent inhibitors of scytalone dehydratase: displacement of a water molecule from the active site. Biochemistry 1998; 37:17735–17744.
55. Kim SW, Cha S-S, Cho H-S, Kim J-S, Ha N-C, Cho M-J, Joo S, Kim KK, Choi KY, Oh B-H. High-resolution crystal structures of Δ^5−3-ketosteroid isomerase with and without a reaction intermediate analogue. Biochemistry 1997;36:14030–14036.
56. Bernstein H, Bernstein C, Payne CM, Dvorakova K, Garewal H. Bile acids as carcinogens in human gastrointestinal cancers. Mutat Res 2005;589:47–65.
57. Samuelsson B. Bile acids and steroids: 96. On the mechanism of the biological formation of deoxycholic acid from cholic acid. J Biol Chem 1960;235:361–366.
58. Sinha SC, Chaudhuri BN, Burgner JW, Yakovleva G, Davisson VJ, Smith JL. Crystal structure of imidazole glycerol-phosphate dehydratase: duplication of an unusual fold. J Biol Chem 2004;279: 15491–15498.
59. Sennett NC, Kadirvelraj R, Wood ZA. Cofactor binding triggers a molecular switch to allosterically activate human UDP-α-D-glucose 6-dehydrogenase. Biochemistry 2012;51:9364–9374.
60. Basarab GS, Steffens JJ, Wawrzak Z, Schwartz RS, Lundqvist T, Jordan DB. Catalytic mechanism of scytalone dehydratase: site-directed mutagenisis, kinetic isotope effects, and alternate substrates. Biochemistry 1999;38:6012–6024.
61. Simanshu DK, Savithri HS, Murthy MR. Crystal structures of *Salmonella typhimurium* biodegradative threonine deaminase and its complex with CMP provide structural insights into ligand-induced oligomerization and enzyme activation. J Biol Chem 2006;281: 39630–39641.